Morphogenesis of a complex glial niche requires an interplay between cellular growth and fusion.

Maria Alexandra Rujano[1], David Briand[1], Bojana Đelić[1,2] and Pauline Spéder[1,*]

1. Institut Pasteur, Brain plasticity in response to the environment, CNRS, UMR3738, Paris, France.
2. Present address: Institut de Biologie de l'Ecole Normale Supérieure (IBENS), Cell Division and Neurogenesis, Ecole Normale Supérieure, CNRS, Inserm, PSL Université Paris, Paris, France

***Corresponding author:**

Pauline Spéder, PhD
Department of Developmental and Stem Cell Biology
Brain plasticity in response to the environment Group
Institut Pasteur/CNRS UMR3738
25 rue du Docteur Roux
75015 PARIS
E-mail : pauline.speder@pasteur.fr
Phone: + 33 1 45 68 89 78.

Abstract

Neural stem cells (NSCs) are found in a tailored, intricate cellular microenvironment, the niche, which supports and regulates their activity. Whilst niche architecture is indissociable from its function, the morphogenetic aspects of niche development have been poorly explored. Here, we use the formation of the cortex glia (CG) network in Drosophila as a paradigm of acquisition of architectural complexity of a NSC niche. CG are essential for normal neurogenesis and build a reticular network spanning the entire central nervous system while encasing each NSC linage. We first show that individual CG cells grow tremendously to enwrap several NSC linages, ultimately covering and tiling the entire tissue. Several proliferative mechanisms, including endoreplication and mitosis, in part acytokinetic, support such growth and result in the formation of multinucleated, syncytial CG cells, that we call units. We then reveal that CG units are able to fuse to each other, resulting in the exchange of several subcellular compartments, such as membrane, cytoplasm and organelles. This process relies on well-known molecular players of cell fusion, involving cell surface communication molecules and actin regulators, while being atypical by its extent, dynamics and partial nature. Ultimately, the coordination in time and space of growth, proliferation and fusion mechanisms is required for the remarkable, multi-level architecture of the Drosophila NSC niche.

Introduction

The central nervous system (CNS) is a complex organ that develops and functions under a range of physiological challenges and homeostatic variations. Throughout life, the generation of new cells in the CNS, a process called neurogenesis, is sustained by neural stem cells (NSC), multipotent progenitors that self-renew while generating more committed precursors that ultimately produce neurons and glia[1–4]. As such, the extent and quality of neurogenesis depends on NSC fitness and proliferative capacity, which must be tightly regulated and balanced. NSC behaviour is regulated by a combination of intrinsic (epigenetics and molecular repertoire) as well as extrinsic biochemical (e.g. growth factors and cytokines) and mechanical (cell contacts and tissue topology) factors provided by the complex cellular microenvironment where NSC reside, the niche[5–7]. In mammals, neurogenic niches comprise multiple cell populations including the NSC themselves, glial astrocytes, neurons, endothelial cells, resident immune cells, blood vessels forming the blood-brain barrier and extracellular matrix[8–10]. They form a functional and physical unit with specific cellular and molecular properties that regulate and support NSC features through integration of cell-cell, paracrine and systemic signals[7,11]. The NSC niche exhibits intricate, tight cellular arrangements, such as astrocytic extensions packed in between and contacting NSCs and blood vessels[8,10]. Direct couplings also exist between several cell types, including between and within progenitor and glia populations, creating complex cellular networks sharing signals[12,13]. The niche starts to form very early during embryogenesis and becomes progressively more elaborate with the progression of neurogenesis and the acquisition of tissue complexity[10,14]. Niche composition and structure must therefore be very dynamic in order to accommodate substantial tissue remodelling that results from neurogenesis during embryogenesis and into adulthood.

Remarkably, we still have scarce understanding on how the structure of the niche is established and how it acquires its 3D organization. Answering these questions requires being able to identify, track and manipulate independently niche cell populations *in vivo*, within their physiological context, conditions that the complexity of the mammalian brain makes challenging to achieve. First, the mammalian NSC niche has a highly heterogeneous cellular composition and architecture. In addition, mammalian models have complex genetics and the existence of multiple, parallel and tractable systems are rare. Finally, while *in vivo* models are a necessity in order to acquire an accurate spatial and temporal picture of the cellular dynamics taking place within a 3D niche, access to a whole living brain in mammals is still a huge challenge. To overcome these issues while offering a system

allowing the investigation of core, conserved cellular and molecular mechanisms supporting NSC niche formation, we use the developing larval Drosophila brain as a model system.

Drosophila NSCs (historically called neuroblasts) are specified during embryogenesis, subsequently delaminate from the neuroectoderm and start proliferating to generate the neurons and glial cells that will form the larval CNS (reviewed in [15–17]). When these primary lineages are completed, the embryonic NSCs exit the cell cycle and enter a quiescent state. Subsequently, during larval development, NSCs are woken up from this dormant phase[18] by a feeding-induced nutritional signal, leading them to enlarge, re-enter the cell cycle and resume proliferation[19–22]. This second wave of neurogenesis lasts until the end of larval life, generating secondary lineages which will make up the majority of the adult CNS.

Proliferating larval NSCs are found in a neurogenic niche which comprises common players, with related functions, to the mammalian niche –namely glial cells, a blood-brain barrier, neurons and the NSCs themselves (Figure 1a). The blood-brain barrier is essential to neurogenesis by relaying the systemic nutritional cues that will trigger NSC reactivation[21,23]. Beneath the blood-brain barrier lie the cortex glia (CG). CG display a striking structure around actively cycling NSCs, individually encasing them and their newborn progeny within membranous chambers while forming a network spanning the whole CNS (Fig. 1a-c)[24–26]. CG perform genuine niche functions. They protect NSCs against oxidative stress[27], can sustain NSCs proliferation under nutritional restriction[28] and are essential for neuronal positioning and survival[24,26,29–31]. Importantly, CG network and NSC encasing (CG architecture) are not present at the beginning of larval life, when NSCs are quiescent. Previous studies have shown that this network forms progressively in response to both nutritional cues and signals from NSCs, pinpointing an exquisite coordination between neurogenic needs, systemic cues and niche morphogenesis[26,32].

Here, we used CG network morphogenesis as a paradigm for niche development and acquisition of architectural complexity. We first addressed the contribution of individual CG cells to network formation and showed that they grow enormously during niche morphogenesis, to eventually tile the entire CNS and encase several NSCs. We then deciphered the exact cellular events supporting CG growth, and found that CG cells proliferate by mitotic division, in part acytokinetic, and also undergo endoreplication, leading to the formation of polyploid, multinucleated cells. In addition, these syncytial cells, that we called CG units, have the ability to fuse to each other, leading to exchange of subcellular compartments, including cytoplasm, membrane, organelles and nuclear content. CG cellular fusion is supported by well-characterised cell-cell recognition molecules as well as actin

regulators. On the other hand, CG fusion appears atypical, as it is partial in nature and seems to be restricted and dynamic in time and space. Finally, we show that CG growth strategies and fusion between CG units are required for correct network architecture. The CG structure, made of connected cells capable of sharing information, and laying in between stem cells and vasculature, is reminiscent of the astrocytic networks present throughout the brain[33]. Our findings provide a novel framework to understand how syncytial, complex reticular structures are formed, as well as a tractable model to decipher the impact of niche structure on NSC functions.

Results

Growth of individual CG cells results in a tiled organization of the cortex glia network

We first sought to visualise the spatiotemporal dynamics of CG network morphogenesis during neurogenesis in the larval CNS. For this, we used either the protein trap Nrv2::GFP that labels CG membranes, or expression of membrane targeted GFP (mCD8::GFP) driven by *cyp4g15-GAL4* (expressed mostly in CG as well as in some astrocyte-like glia, readily identifiable based on morphology and dorsal compartmentalisation, see Supp. Fig S1a). In accordance with CG chambers being progressively formed in parallel with NSC reactivation[26], the CG network starts as a loose, gaping meshwork at ALH0 (ALH: after larval hatching) that progress to a highly interconnected reticular network around ALH48, when it encloses each individual NSCs (Figure 1c-d, shown in the ventral nerve cord, VNC). Eventually, the CG network spans the entire tissue at ALH96. Network growth and acquisition of complexity is associated with dramatic changes in the size and morphology of CG cells, that extend their membranes to gradually accommodate the growing NSC lineages (Figure 1d). Remarkably, the resulting intricate network efficiently maintains the individualities of each NSC lineage.

Next, we determined the contribution of each individual CG cell to network formation and NSC encapsulation. We expressed in CG the multicolour lineage tracing tool Raeppli[34], that contains one single copy of membrane targeted Raeppli (Raeppli-CAAX) and can be induced at the desired time upon Flippase (FLP) recombination (Supp. Fig S1b). Its induction just After Larval Hatching (ALH0-2) resulted in the expression of exclusively one of four different colours in the young CG cells. Generated clones extended from ALH0 to ALH96, spanning the whole tissue and forming clear boundaries between them, ultimately tiling the entire brain (Figure 1e). A similar tiled organisation was observed previously, using stochastic expression of two fluorophores, around primary mature neurons[29]. We quantified the volume of individual clones over time (Figure 1f) and found a steady growth of single colour clones from ALH0 to ALH96, with the most significant increase between ALH72 and ALH96 in concomitance with NSC lineage expansion. Remarkably, we also observed that each single CG clone (derived from one single CG cell) can encase several NSC lineages (Figure 1g), ranging from 5 NSCs per clone at ALH48 to an average of 10 NSCs per clone at ALH72 (Figure 1h). All together these results show that CG are able to grow until entirely tiling the brain while precisely encapsulating several NSC lineages.

CG cells exhibit multiple cell cycle strategies

We then asked about the cellular mechanisms at play to support such extensive clonal growth. Two powerful, rather opposite strategies can fuel the generation of large clones. Mitosis results in both cellular and nuclear divisions and thus leads to increased cell numbers. On the other hand, endoreplication results in increased DNA content (i.e., polyploidization) without cellular division, and results in larger cell size[35–37].

CG proliferation has been reported previously based on CG nuclei counts, either in clones or in specific CNS region[25,29,38]. However, the cell cycle mechanisms supporting such proliferation, as well as the resulting cellular organization remained debated. While increased nuclei numbers suggested mitotic events, there were also evidence fitting endoreplicative processes, such as polyploidy detected at early stages[32]. We thus decided to do a thorough examination of the cell cycle in CG.

We first confirmed that CG nuclei numbers in the entire CNS largely increase between ALH48 and ALH96, after NSC encasing, suggesting that proliferation is enhanced when NSC lineages are expanding (Supp. Fig. S1c-d). To determine the contribution of the individual CG cells present at ALH0 to this increase, we induced Raeppli-CAAX clones at ALH0 and stained for the pan-glial marker Repo (Supp. Fig. S1e). Counting the number of $Repo^+$ nuclei in each CG clone revealed a fivefold increase between ALH48 and ALH96 (Supp. Fig. S1f), in accordance with whole CNS count.

We then used the genetic tool Fly-FUCCI that allows to discriminate between G1, S and G2/M phases[39] to assess CG cell cycling activity along network formation, focusing on the VNC for simplicity (Fig. 2a-b). FUCCI relies on a combination of fluorescently-tagged degrons from Cyclin B and E2F1 proteins which are degraded by APC/C and $CRL4^{CDT2}$ from mid-mitosis and onset of S phase, respectively (Supp. Fig S2a). While CG nuclei appeared mostly in G1 at ALH0, we observed a progressive increase in the number of nuclei in S and G2/M between ALH24 and ALH72, followed by a sharp return to G1 at ALH96 (Fig. 2a-b), a temporal pattern reminiscent of the timing and level of NSC proliferation overtime. We also noticed that such change in cell cycle profile followed an antero-posterior pattern (compare ALH24 with ALH48 in Fig. 2a). This suggests that at least part of the CG population cycles between replicative and gap or mitotic phases, and that such cycling is spatially regulated and temporally coordinated with NSC behaviour.

To assess whether CG cells undergo proper mitosis, we checked *bona fide* mitotic hallmarks. We first stained CG cells with the mitotic marker phospho-histone H3 (PH3), at different time points (Fig. 2c-d) and detected $PH3^+$ CG cells between ALH24 and ALH72, paralleling the window of FUCCI with more CG cells in S or G2/M phases. Next, by

performing live-imaging of RFP-tagged histone (*Hist::RFP*) driven by *cyp4g15-GAL4* on whole brain explants (see Methods), we were able to observe DNA condensation, metaphase alignment and chromosomes' segregation (Fig. 2e, Movie S1). Moreover, we observed nuclear envelope breakdown followed by reformation using *Lamin::GFP* driven by *cyp4g15-GAL4* (Supp. Fig. S2b, Movie S2). We also looked at the behaviour of the Drosophila homolog of anillin (*scraps, scra*), a conserved scaffolding protein involved in late stages of cytokinesis[40]. Anillin is found in the nucleus during interphase, relocates to the contractile ring during cytokinesis [41], and forms part of the midbody, a contractile ring-derived microtubule-rich proteinaceous structure assembled at the intercellular bridge between the two daughter cells at the end of mitosis and that marks the abscission site. Expressing RFP-tagged anillin in CG (*mRFP::scra)* uncovered midbody-like structures in between recently divided CG (Fig. 2f, identified by a decrease in nuclear-localised anillin compared to neighbouring CG nuclei) and midbody remnants along the CG membranes (Supp. Fig S2c). Quantifying anillin-positive midbody structures along time (Fig. 2g) revealed an increase between ALH48 and ALH96, similarly to CG nuclei counts. All together, these data suggest that CG cells do undergo proper mitosis, including nuclear division and cytokinesis.

Next, we sought to address whether endoreplication and subsequent polyploidization could also happen in CG. We assessed CG ploidy through DNA Fluorescence *In Situ* Hybridization (FISH) on chromosomes II and III (two out of the four Drosophila chromosomes[42]), and counted chromosome numbers in labelled CG nuclei along development (Figure 2h-i). We observed that at early stages, CG have a normal ploidy of 2n, which increases at ALH72 (average ~4n, with a maximum of 10 and 9 FISH signals for chromosome 2 and 3, respectively) for part of the CG population, and decreases again to 2n at ALH96. Although we cannot exclude that part of this increase corresponds to catching DNA replication before mitosis ($PH3^+$ staining also peaks at ALH48-72, Fig. 2d), odd numbers as well as n>4 imply a contribution of polyploidization. Importantly, CG-specific downregulation of Dup (*double parked* gene), a DNA replication protein shown to be crucial for endoreplication[43,44], caused a strong reduction in CG nuclei size and number (Figure 2j) and resulted in severe defects in CG growth and network morphogenesis (Fig. 2k). Notably, endoreplication covers two cell cycle variants[35,45]. Endocycle alternate DNA replication (S-phase) with a gap (G) phase and do not shown any mitotic features. Endomitosis includes S phase and some aspects of mitosis up to telophase[46], but do not complete cellular division. Interestingly, by live-imaging on whole brain explants we were able to observe endomitotic events, characterized by entry

into mitosis followed by chromosomes segregation, but absent later mitotic stages, and instead the DNA collapses back into only one nucleus (Figure 2l, Movie S3). All together, these data show that polyploidization does occur in CG in a temporary fashion, in some cases through endomitosis, and is essential for network formation.

CG glia are syncytial units

While CG displayed well-characterized marks covering different mitotic steps, we also noticed peculiar behaviours that indicated a subtler picture. First, using live-imaging to record CG division, we noticed that mitoses often appeared synchronised between several nuclei (Fig. 3a, Movie S4). Similarly, using Fly-FUCCI, groups of neighbour nuclei were found at the same cell cycle phase (Fig. 3b). Moreover, we observed that several close-by CG nuclei were undergoing cytokinesis at the same time (anillin displaced from nuclei and accumulating in intercellular bridges), even sometimes seemingly linked by anillin cytoplasmic staining (Fig. 3b). Such coordinated behaviour between a group of CG nuclei suggest that they are receiving the same cell cycle cues. We thus wondered whether multiple CG nuclei could actually be sharing cytoplasmic material.

To test this hypothesis, we used a Fluorescence Loss In Photobleaching (FLIP) technique, an approach used to examine the movement of molecules inside a cell and that can also serve to assess the continuity of a cellular compartment (reviewed in [47,48]). FLIP relies on the continuous bleaching of a small region of a fluorescently-labelled cell, while recording the entire zone whose continuity is being assessed. The continuous illumination will result not only in the bleach of the targeted region, but also will lead to the loss of fluorescence in any connected area, due to molecular diffusion. In contrast, non-connected area will not be bleached. To assess whether CG cells share cytoplasmic material, we expressed cytoplasmic GFP and RFP-tagged histone (*Hist::RFP*) in the entire CG population and imaged an area containing several CG nuclei. We then repetitively bleached GFP in a small region of the cytoplasm and recorded the loss of fluorescence with respect to CG nuclei. Strikingly, we were able to observe loss of fluorescence in large areas containing several CG nuclei (Fig. 3c and Supp. Fig. S3), implying that indeed these CG nuclei are part of a continuous, connected cytoplasmic compartment. Quantifying FLIP experiments at different times revealed that the average number of connected CG nuclei increases twofold along CG network formation (Fig. 3d; average ALH24 = 3, versus average ALH96 = 7). These experiments show that CG cells are thus multinucleated.

Endomitosis could produce multinucleated cells in the rarer case they go through nuclear envelope breakdown and reformation. Nevertheless, the simplest explanation to account for

such an extent of multinucleation would be that CG undergo mitosis but fail to complete cytokinesis. The midbody is indeed a temporary structure formed between the two daughter cells during cytokinesis and that has a role in recruiting abscission proteins. Until recently, it was thought that the midbody was fated to being cleaved and discarded after abscission, but more recent studies have shown that midbodies can be retained or even up-taken by surrounding cells and have functions beyond abscission[49]. Interestingly, counting anillin-enriched midbody structures localised along CG membranes revealed a steady increase in numbers over time (Fig. 2g), what entails that they are not discarded but rather remain. This suggests that CG cells that enter mitosis but fail cytokinesis might stay connected by the intercellular bridge and the midbody. To demonstrate this possibility, we performed FLIP, expressing a cytoplasmic GFP together with mRFP::scra in all CG cells (Fig. 3e). We repetitively bleached GFP in a small cytoplasmic region next to an isolated RFP^+ punctum localised in a narrow cytoplasmic extension between CG nuclei. We found that the loss of fluorescence was able to propagate through the RFP^+ punctum, reaching CG nuclei localised on the other side. All together, these data show that CG cells are multinucleated and form syncytial compartments, in part through incomplete cytokinesis that will leave connections via the midbody/intercellular bridge. From now on, we will call these syncytial structures, CG units.

CG units can undergo cellular fusion

Using multicolour clonal analysis with membrane targeted Raeppli, we showed that individual CG cells give rise to neighbouring units with well-defined boundaries that tile the CNS, while maintaining NSC lineages individualities (Fig. 1e, g). Intriguingly, we were also able to observe membrane areas with colours overlap (Fig. 4a), that slightly increased over time (Supp. Fig. S4a-b). The partial, not complete nature of the overlap, as well as colour induction well before detected polyploidization (see Fig. 2i), excluded that such event would come from polyploid cells harbouring multiple copies of the genetic tool. We thus wondered whether sharing of colours between two neighbouring units could be a result of cell-cell fusion.

Cellular fusion is the process by which two cells will merge their membranes into a single bilayer, resulting in the exchange of their cytoplasmic content and subcellular compartments (organelles, nuclei). Cell-cell fusion is a fundamental process during development (fertilization), formation of tissues (such as the muscle or the placenta) and for immune response[50]. In addition, an increasing number of evidence links the unwanted occurrence of cell fusion to pathological mechanisms, such as cancer progression and pathogenic

infection[51,52]. Cell fusion is a stepwise process (reviewed in[53–56]). First cells become competent for fusion, usually with one donor and one acceptor. They then adhere to each other through cell recognition molecules. Membrane hemifusion proceeds, mediated by fusogens and actin remodelling that ultimately leads to pore formation. Cells start to exchange their cytoplasmic content through the pore, which becomes wider, and eventually fully integrate, sharing all their compartments.

We first wondered whether such partial colour overlap between clones could be detected for cellular compartments other than the plasma membrane. We took advantage of the CoinFLP technique, which allows the stochastic labelling in two colours of individual cells within the same population (Supp. Figure S4c)[57]. A bias in the system results in the generation of a minority of well-sparse clones in one of the two colours, making them easy to localise and quantify. Early induction of this tool in CG cells using *cyp4g15-FLP* (which is active before ALH0, see Methods) and two differently-labelled fluorescent cytoplasmic markers (GFP and mCherry), generated three situations (Fig. 4b-c): i) a majority of clones of only one colour (GFP only, green); ii) clones fully colocalising with the other colour (GFP + mCherry complete overlap, grey); and iii) a minority of clones partially colocalising with the other colour (GFP + mCherry partial overlap, grey-hashed green). While full overlaps might come from polyploidy, the occurrence of partial cytoplasmic overlaps fitted the hypothesis of fusion between CG units. We then performed a similar experiment using this time fluorescently-labelled mitochondrial markers, and also found partial colocalisation in a small number of cases (Supp. Fig. S4d), suggesting that two CG units from different origins can share these organelles. Finally, we used a nuclear-tagged version of Raeppli (Raeppli-NLS) to identify the nuclei belonging to different CG units. While we observed clones of neighbouring nuclei with an organisation reminiscent of what was seen with Raeppli-CAAX, and confirming clonal expansion of individual CG cells (Supp. Fig. S4e), we also found intriguing overlaps at the border of clones, with few nuclei exhibiting two colours showing qualitative inverse intensities (Suppl. Fig. S4f). This suggests that nuclei from different CG units in close vicinity can exchange nuclear targeted proteins. All together, these data show that CG units can share subcellular compartments, including plasma membrane, cytoplasm, mitochondria and nuclei.

Cell fusion entices that information/signals could propagate from one cell to the other up to the end of the fused area. To test this hypothesis, we combined the identification of zones of partial cytoplasmic overlap through CoinFLP (see Fig. 4b; GFP and mCherry) with a FLIP approach in live-imaging. Continuous bleaching of one colour (GFP) in a small region of one

of the two CG units, outside of the overlapping zone (Fig. 4d) led to a loss of fluorescence not only in the CG unit targeted by the bleaching, but also in the overlapping area (GFP + mCherry), up to the border with the other unit (mCherry alone). This shows that the overlapping zone between the two CG units is indeed in cytoplasmic continuity with at least one individual unit. This demonstrates that overlapping subcellular compartments between CG units correspond to zones of signal exchange.

Another prediction arising from the occurrence of cellular fusion between CG units, already multinucleated, would be that they actually create even bigger cellular compartments, with a continuity of information and containing nuclei from different origins. To test this hypothesis, we performed FLIP on CG expressing a cytoplasmic fluorescent marker (GFP) in the whole population together with stochastic multicolour nuclear labelling (Raeppli-NLS) induced early, hence leading to differently labelled clonal CG units (such as seen in Supp. Fig 4e). Continuous bleaching in a small area of the cytoplasmic GFP surrounding one of the CG clones resulted in a loss of fluorescence not only in the targeted CG clone, but also in its adjacent neighbour (Fig. 4e). We observed this event in a number of CG units with diverse organisation (see Supp. Fig. 4g for another example), making the observation reproducible qualitatively while difficult to assess quantitatively. From these data, we can conclude that CG units can fuse and generate larger connected areas, leading to exchange of subcellular compartments and associated signals at a much larger spatial scale.

Cell fusion between CG units is regulated by canonical fusion molecules

Cell-cell fusion relies on cellular and molecular mechanisms allowing one partner to invade the other. A biological model which has been highly instrumental in deciphering fusion hallmarks is the generation of myofibers in Drosophila (reviewed in[58–60]). In this model (Supp. Fig. S5a), a fusion-competent myoblast (FCM) and a founder cell (FC) recognize and bind to each other, creating a so-called fusogenic synapse. Key, well-characterized players for this step are the cell recognition and adhesion molecules that mediate the binding between the two membranes. These molecules often contain an immunoglobulin domain and are differentially localised in the fusing cells, expressed either by the FCM (Sns and Hbs) or by the FC (Kirre/Duf and Rst). Binding between partners initiate further intracellular signalling, through adapter proteins (*i.e.*, Rols7/Ants in FC and Dock in FCM), that will lead to remodelling of the actin cytoskeleton in both cells, however in different fashions. In the FCM especially, the combined actions of multiple actin regulators (WASp, Rac, Scar, Arp2/3 to name a few) generate invasive podosome-like protrusions at the interface with the FC. These structures trigger a Myosin II- and spectrin-mediated response in the FCs, which is

followed by hemifusion of membranes and pore formation, which is then stabilized and expanded to culminate the process. The end point is the creation of a multinucleated cell, the muscle fiber. We wondered whether similar cellular events and molecular players were involved in fusion between CG units.

First, using live-imaging, we assessed whether we could observe dynamic cellular behaviour at the border between adjacent CG units. Using two differently-labelled fluorescent cytoplasmic markers in a CoinFLP set up in the CG, we indeed observed active protrusion-like structures tunnelling into the reciprocal cells (Fig. 4f). This suggests that some cellular remodelling takes place at the interface between two fusing CG units.

Next, we asked whether known molecular players of myoblast fusion were expressed and required for fusion between CG units. Notably, most players are differently expressed between the two fusing cells. In light of the restricted and for now spatially unpredictable occurrence of fusion events in the CG, we decided to first focus on molecular players known to be expressed in the two partners. We turned to Myoblast City (*mbc*), a Guanine nucleotide Exchange Factor (GEF) implicated in actin remodelling and known to be expressed, if not required[61], in both the FC and the FCM (Supp Fig. S5a). We first took advantage of a genomic trap line inserting a GAL4 driver under the control of *mbc* enhancers, creating a Trojan *mbc-GAL4*[62,63]. Driving both a nuclear (Hist::RFP) and membrane reporter (mCD8::GFP) revealed a strong expression in the CG (co-stained with the glial marker Repo), reproducing the characteristic CG meshwork pattern (Fig. 5a). Moreover, expressing lineage tracing tools (i-TRACE[64] and G-TRACE[65]) under *mbc-GAL4* indicated that *mbc* is expressed in the CG throughout development (Supp. Fig. S5b-d). *mbc* expression in the CG was further confirmed by immunostaining with an anti-Mbc antibody, whose staining was enriched along the CG membranes (Fig. 5b). Importantly, such enrichment was lost upon *mbc* RNAi-mediated downregulation in the CG (Fig. 5b). Of note, both *mbc-GAL4* and Mbc antibody showed that *mbc* was expressed in other cell types, notably the surface glia and astrocyte-like glia, as well as in a few neurons (data not shown). Importantly, we were able to detect a faint staining for the adhesion molecule Kirre, which colocalised with a marker for the CG membrane and which was lost under *kirre* knockdown in the CG (Fig. 5c). All together, we show that Mbc and Kirre, two known regulators of myoblast fusion, are expressed in the CG during larval stages.

We then asked whether *mbc*, as well as other molecular players associated with myoblast fusion, were required for fusion between CG units. We independently knocked down several fusion genes in the CG through RNAi while inducing multicolour clonal labelling (Raeppli-

CAAX) and calculated the number of fusion events (overlap between at least two colours, see Methods) per VNC compared to a control condition (Fig. 5d). Strikingly, we observed a significant reduction in the number of fusion events when either *mbc*, *Wasp*, *hbs* or *rst* were knocked down (Fig. 5e). For *mbc* and *Wasp*, which showed the most significant reductions, this was paired with a slight increase in number of clones per VNC (Fig. 5f), in accordance with preventing the generation of larger CG units. *sns*, *kirre* and *lmd* knockdowns also tended towards a reduction in the number of fusion events, albeit the difference was not statistically significant (Fig. 5d-e and Supp. Fig. S6a-c). These data show that known molecular players of classical fusion pathways regulate fusion of CG units.

Cellular fusion of CG units is required for correct CG architecture

Our results have shown that fusion does occur between CG units, at a relatively low rate. We enquired about the functional relevance of such events for the structure and function of the CG. To do so, we took advantage of our data identifying molecular regulators of fusion between CG units (Fig. 5) and assessed the impact of knocking them down in the CG.

We observed that individually knocking down fusion genes resulted in alterations of the overall CG network structure, although ranging in magnitude (Fig. 6a and Supp. Fig. S6d). We first observed localised disruptions or alterations in chamber shapes for *mbc*, *dock* and, in a lesser extent, for *kirre*, *sns* and *lmd* (see arrows). In particular, we noticed in *mbc* RNAi some heterogeneous distribution of the CG membrane, with local accumulation or rather fainter signal or restricted gap (Fig. 6a). Meanwhile, *WASp* RNAi led to a dramatic disorganisation of the CG network, with destruction of NSC chamber structure and loss of membrane coverage along the network, something we also observed through Raeppli CAAX (Fig. 5c). As WASp is a general regulator of actin cytoskeleton, by enabling actin nucleation for microfilament branching, it is possible that its effects bypass its strict involvement in fusion mechanisms, leading to stronger phenotypes. Taken these observations together, we propose that fusion genes are important for refining/precise CG network and chamber organisation.

Discussion

Here we dissect the cellular mechanisms supporting the acquisition of architectural complexity in the Drosophila NSC niche using the morphogenesis of the CG network as a paradigm. We have first uncovered that individual CG cells grow extensively during niche formation, becoming both polyploid and multinucleated through events of endoreplication and acytokinetic mitosis. As such they form syncytial units in which the different nuclei stay connected, some of which through cytoplasmic bridges as visualized by residual midbodies. We found that these CG units enwrap several NSCs and mostly form neat membrane boundaries between each other, covering the entire CNS in a tile-like fashion. Furthermore, we revealed that CG units can also fuse with each other, relying on classical pathways involving adhesion molecules and actin regulators. This fusion results in the exchange of several subcellular compartments, including cytoplasm and organelles, between the CG units involved. Ultimately, the combination of cellular growth, proliferation and fusion are required to build CG niche architecture (Fig. 6b).

Polyploidy has been associated with large cells or cells that need to be metabolically active, as a way to scale their power of biosynthesis to their cellular functions (reviewed in[37,46]). For example, the megakaryocytes of the bone marrow, which are required to generate large quantities of mRNA and protein for producing platelets, undergo polyploidization. Polyploidy is also an elegant way to support cell growth while protecting a specific cell architecture that would suffer from mitosis-associated adhesion and cytoskeleton changes. In this line, the polyploidization of the subperineurial glia, which exhibit strong junctions to fulfil its role as a blood-brain barrier, has been shown to maintain barrier integrity in response to CNS growth[43]. The CG cells, which have a highly complex topology integrating NSC position and display large sizes (Fig. 1f) fits both categories.

Importantly, increase in ploidy can be achieved by different processes, many of which rely on variations of the cell cycle[35,36,45,66], including endocycle (alternance of S and G phases without chromosome segregation), endomitosis (alternance of S and G phases with partial mitotic progression, generally until anaphase) and acytokinetic mitosis (mitosis without abscission). Here we propose that CG exhibit several cycling strategies to increase their ploidy. The increase in chromosome number seen in some nuclei (Fig. 2h-i) as well as some aborted DNA segregation at anaphase (Fig. 2l) imply that CG undergo either endocycling or endomitosis without nuclear division. In addition, some CG perform acytokinetic mitosis, displaying all stages of mitosis including intercellular bridges and midbody formation (Fig. 2c-d, f-g and Supp. Fig. S2b), but without abscission, leading to a syncytial, multinucleated

unit of CG cells (Fig. 3e). We cannot exclude that some CG cells complete mitosis and undergo proper cell division, an outcome challenging to observe considering CG architecture. Interestingly, acytokinetic mitosis is reminiscent of what happens in the germline stem cell niche of many animals[67], including in Drosophila in which the maturing oocyte and supporting nurse cells stay connected by ring canals, intercellular bridges that, instead of undergoing abscission, are stabilized on arrested cleavage furrows[68]. Notably, blocking endoreplication is detrimental to network formation (Fig. 2k), whereas preventing the increase in CG nuclei (through knockdown of string/*cdc25*, what prevents mitotic entry, or expression of the cyclin E/cdk2 inhibitor *dacapo*, what blocks G1 to S transition) did not have any detectable impact[26], a puzzling observation. How the balance between endoreplication and mitosis is regulated, as well as more generally the trigger(s) and timing for these processes are the next key questions that need to be addressed. The antero-posterior wave of CG cycling (Fig. 2a) is particularly intriguing. Notably, it was shown before that CG proliferation depends on nutrition via activation of the PI3K/Akt pathway[26,38], also a crucial regulator of NSC exit from quiescence during early larval development. The interplay between spatial and temporal signalling will thus be of special interest.

Using several approaches, including dual and multicolour clonal analysis for different subcellular compartments, FLIP experiments and targeted loss of function, we have shown that CG units have the ability to interact with each other and share their components in a manner dependent of known molecular players in myoblast fusion. A puzzling observation is the spatially-limited nature of this exchange, as witnessed through cytoplasmic and membrane markers (Fig. 4a-d). Our data indeed support the existence of atypical fusion events, partial in nature, dynamic in time and plastic in space. Complete, classical cell-cell fusion is expected to lead to full mixing of all components in time. Although some compartmentalisation between components of the two cells of origin could still be happening, depending on mixing properties (i.e., membrane proteins; phase separation) or fixed positioning (i.e., nuclei), cytoplasmic contents at least should be fully combined, homogeneously or at least in a gradient manner, per diffusion laws. However, we are able to observe sharp boundaries between fused (*i.e.*, colour overlap) and unfused (one colour) regions (Fig. 4a-b). A possibility could be that we catch the event at a very early stage. However, in this case we should expect some complete colour overlap at later stages, at least at the same frequency with which partial mixing happened at the previous recorded stages, something we do not see (see Fig. 1e, ALH96, representative of the rarity of complete overlaps at this stage). A fitting explanation could be that the fusion happening

between CG cells is somehow transient, and that other, unknown mechanisms exist to rupture and close membranes again, severing the communication between the two original CG units, either on one side or in both. The boundary between CG units would be flexible, behaving like a moving barrier and creating mixed CG domains as remnants. Interestingly, there has been some previous reports of partial cell fusion (discussed in[69]), suggesting that such phenomenon might be underestimated and possibly hidden. For example, partial cellular exchange of proteins and organelles has been documented between stem cell and differentiated cells (cardiomyocytes), a phenomenon leading to nuclear reprogramming of the differentiated cells[70]. One of the proposed cellular bases for such partial exchange is through the establishment of tunnelling nanotubes, which are thin and long membranous, actin-based protrusions, that connect and offer a compartmental continuity between two, often distant, cells[71,72]. Actually, the exact cellular mechanisms at play during fusion between CG units remain to be precisely identified. Although the involvement of at least some of the molecular players controlling myoblast fusion suggests shared adhesion and actin-dependent mechanisms, whether similar asymmetry in cell players (*e.g.*, fusion competent cells versus founder cells), molecular interactions and intracellular signalling happen in CG is left to be demonstrated. Recently, full cytoplasmic exchange between cells of the Drosophila rectal papillae have been shown to happen through membrane remodelling and gap junction communication rather than classical fusion pathways[73]. Interestingly, we sometimes observe a lesser intensity of one of the fluorophores in the shared, fused zone, at least for membrane (see Fig. 4a), suggesting that material exchange might not be homogeneous, and rather directional and/or controlled. Ultimately, the exact nature of the fusion between CG units remains to be thoroughly investigated.

The parameters regulating the frequency, location and timing of these atypical fusion events also remain mysterious. A way to understand when and where fusion happens might be to understand why it happens. Here we show that fusion between CG units is required for a gapless, seemingly-continuous meshwork (Fig. 6a). Beyond a more generic role of the actin cytoskeleton in CG architecture, as hinted with WASp phenotype, this could suggest that CG fusion somehow ensures that no gap in CG network and in the associated coverage of NSCs is left unmet. A first hypothesis would be that fusion acts as a rescue mechanism, kicking in when tiling between CG units fails. Fusion evens can indeed be triggered in stress situations, as a fast adaptive mechanism[74]. Another option would see fusion as a strategy to modulate the extent of communication and signal exchange within the CG network, as a response either to CG own fluctuating needs or to NSC behaviour, fulfilling its role as a

neurogenic niche. In this line, we noticed a slight fluctuation in the number of fusion events (Supp. Fig. S4b), as well as in the number of NSCs encased by one CG unit overtime (Fig. 1h, decrease between ALH72 to ALH96), hinting that remodelling of CG unit boundaries through fusion might be a way to control niche properties along neurogenesis.

Here we show that a glial, reticular network is built from cell growth and cell fusion mechanisms, resulting in a highly connected structure which enwraps NSC. Although the exact same topology might not be found in mammals, it is interesting to note that astrocytes have been shown to set up gap junctions between them, becoming a so-called astrocytic syncytium[75,76]. Moreover, astrocytes in the mammalian NSC niche form, through their end feet, a reticular structure sitting between neural progenitors and the blood vessels [9], similarly to the *glia limitans* between the meninges and the cerebral parenchyma[77]. This suggests that connected glial networks, regardless of the exact mechanism building their properties, might be a common occurrence during CNS development. In addition, increasing evidence pinpoints the existence of fusion-based cell-cell communication in the mammalian brain[78,79], as well as restricted polyploidy, such as in Purkinje neurons. Understanding the features and regulators of CG morphogenesis, as well as the resulting roles on neurogenesis, thus provides an original blueprint to explore several aspects of morphogenetic processes of complex structures, fully within as well as beyond the neurogenic context.

Methods

Fly lines and husbandry

Drosophila melanogaster lines were raised on standard cornmeal food at 25°C. Lines used in this study are listed in the table below:

Strains	Source	Stock number/Reference
w^{1118}	BDSC	5905
Nervana2::GFP (Nrv2::GFP)	BDSC	6828
tubulin-GAL80$^{thermosensitive(ts)}$	BDSC	65406
Cre recombinase	BDSC	851
yw, hs-FLP	A. Brand lab	
CoinFLP	BDSC	58750
cyp4g15-GAL4	BDSC	39103
cyp4g15-FRT-STOP-FRT-LexA	This study	
cyp4g15-FLP	This study	
alrm-GAL4	Marc Freeman lab	[80]
mbc-GAL4 (Trojan)	BDSC	66840
UAS-H2B::YFP (Hist::YFP)	F Schweisguth lab	[81]
UAS-H2B::RFP (Hist::RFP)	Y Bellaïche lab	[82]
UAS-His3.3.mIFP-T2A-HO1 (Hist::IFP)	BDSC	64184
UAS-GFP	BDSC	1522
UAS-mCD8::GFP	BDSC	5130
UAS-mCD8::RFP	BDSC	27399
UAS-mito::GFP	BDSC	8443
LexAOp-mCherry::mito	BDSC	66531
UAS-Raeppli CAAX 43E	BDSC, This study	55082
UAS-Raeppli NLS 53D	BDSC, This study	55087
LexAop-Raeppli CAAX 43E	BDSC, This study	55082
UAS-mRFP::Scra	BDSC	52220
Fly FUCCI	BDSC	55117
G-TRACE	BDSC	28280
iTRACE	BDSC	66387
UAS-mbc RNAi	BDSC	32355
UAS-WASp RNAI	BDSC	51802
UAS-rst RNAi	VDRC	27223
UAS-hbs RNAi	BDSC	57003
UAS-kirre RNAi	VDRC	27227
UAS-lmd RNAi	BDSC	42871
UAS-sns RNAi	BDSC	64872
UAS-dock RNAi	BDSC	27728
UAS-dup RNAi	BDSC	29562

Larval staging

Embryos were collected within 2-4 hours window on grape juice-agar plates and kept at 25°C for 20-24 hours. Freshly hatched larvae were collected within a 1 hour time window (defined as 0 hours after larval hatching, ALH0), transferred to fresh yeast paste on a standard cornmeal food plate and staged to late first instar (ALH24), late second instar (ALH48), mid third instar (ALH72) and late third instar (ALH96).

DNA cloning and Drosophila transgenics

A portion of the *cyp4g15* enhancer (GMR55B12, Flybase ID FBsf0000165617), which drives in the cortex glia and (some) astrocyte-like glia, was amplified from genomic DNA extracted from *cyp4g15-GAL4* adult flies, with a minimal Drosophila synthetic core promoter [DSCP[83]] fused in C-terminal.

For creating *cyp4g15-FLP*, the *FLP* DNA, which codes for the flippase enzyme, was amplified from the plasmid pMH5[84] (Addgene 52531). This amplicon together with the *cyp4g15^{DSCP}* enhancer were joined using the Multisite gateway system[85] in the destination vector pDESThaw sv40 gift from S. Stowers) in order to generate a *cyp4g15^{DSCP}-FLP* construct. The construct was integrated in the fly genome at an attP18 docking site through PhiC31 integrase-mediated transgenesis (BestGene). Several independent transgenic lines were generated and tested, and one was kept (*cyp-FLP*).

For creating *cyp4g15-FRT-STOP-FRT-LexA*, a FRT STOP cassette was amplified from an UAS-FRT.STOP-Bxb1 plasmid (gift from MK. Mazouni) and the LexA sequence was amplified from the entry vector L2-LexA::p65-L5 (gift from M. Landgraf). The two amplicons were joined together by overlapping PCRs. This *FRT-STOP-FRT-LexA* amplicon together with the *cyp4g15^{DSCP}* enhancer were inserted in the destination vector pDESThaw sv40 using Multisite gateway system[85] to generate a *cyp4g15^{DSCP}-FRT-STOP-FRT-LexA::p65* construct. The construct was integrated in the fly genome at an attP2 or attP40 docking sites through PhiC31 integrase-mediated transgenesis (BestGene). Several independent transgenic lines were generated and tested, and one was kept for each docking site.

Generation of UAS-Raeppli and LexAOp-Raeppli lines

The original construct (BDSC 55082), placing Raeppli CAAX under the control of both UAS and LexAOp sequences, was crossed to a Cre recombinase line (BDSC 851) to randomly excise one of the two control sequences. The resulting lines were checked by PCR to determine whether they carried the UAS or LexAop version.

A similar protocol was followed to generate UAS-Raeppli NLS 53D and LexAOp-Raeppli

NLS 53D constructs from the original line BDSC 55087.

Fixed tissue Immunohistochemistry and imaging

For immunohistochemistry, CNS from staged larvae were dissected in PBS, fixed for 20 min in 4% formaldehyde diluted in PBS with 0.1% Triton X-100, washed two times in PBS-T (PBS+0.3% Triton X-100) and incubated overnight at 4°C with primary antibodies diluted in PBS-T. After washing three times in PBS-T, CNS were incubated overnight at 4°C with secondary antibodies (dilution 1:200) and DAPI (1:1000) diluted in PBS-T. Brains were washed three times in PBS-T and mounted in Mowiol mounting medium on a borosilicate glass side (number 1.5; VWR International). Primary antibodies used were: guinea pig anti-Dpn (1:5000, in-house made, using pET29a-Dpn plasmid from J. Skeath for production), rabbit anti-Dpn (1:200, gift from R. Basto), chicken anti-GFP (1:2000, Abcam ab13970), rat anti-ELAV (1:100, 7E8A10-c, DSHB), mouse anti-Repo 1:100 (DSHB, 8D12-c), rabbit anti-Phospho-histone H3 (1:100, Millipore 06-570), rat anti-mbc (1/200), guinea pig anti-kirre (1/1000). Fluorescently-conjugated secondary antibodies Alexa Fluor 405, Alexa Fluor 488, Alexa Fluor 546 and Alexa Fluor 633 (ThermoFisher Scientific) were used at a 1:200 dilution. DAPI (4′,6-diamidino-2-phenylindole, ThermoFisher Scientific 62247) was used to counterstain the nuclei.

Image acquisition and processing

Confocal images were acquired using a laser scanning confocal microscope (Zeiss LSM 880, Zen software (2012 S4)) with a Plan-Apochromat 40x/1.3 Oil objective. All brains were imaged as z-stacks with each section corresponding to 0.3-0.5 μm. Images were subsequently analysed and processed using Fiji (Schindelin, J. 2012), Volocity (6.3 Quorum technologies), the Open-Source software Icy v2.1.4.0 (Institut Pasteur and France Bioimaging, license GPLv3) and Photoshop (Adobe Creative Cloud).

Live imaging

For live imaging, culture chambers were prepared by adding 300 μl of 1% low-melting agarose prepared in Schneider's medium supplemented with pen-strep on a glass-bottom 35 mm dish (P35G-1.5-14-C, MatTek Corporation) and allowed to solidify. Circular wells of aproximately 2 mm diameter were then cut out using a 200 μl pippet tip fitted with a rubber bulb. CNS from staged larvae were dissected in Schneider's Drosophila medium (21720-024, Gibco) supplemented with 10% heat-inactivated fetal bovine serum (10500, Gibco), penicillin (100 units ml^{-1}) and streptomycin (100 μg ml^{-1}) (penicillin–streptomycin 15140,

Gibco). 4–6 CNS were placed inside small wells of a pre-prepared culturing chamber and covered with culture medium (Schneider's + 5 % FBS + larval lysate (10 µl/ml) + pen/strep (1/100). Larval lysate is prepared by homogenising twenty 3rd instar larvae in 200 µl of Schneider's, spinning down once at 6000 rpm for 5min at 4°C, and recovering the supernatant. Brains were set in position and let to settle around 5-10 minutes before starting imaging. Brains were imaged on a laser scanning confocal microscope (Zeiss LSM 880, Zen software (2012 S4)) fitted with a temperature-controlled live imaging chamber (TC incubator for Zeiss Piezo stage, Gataca systems) using a Plan-Apochromat 40x/1.3 Oil objective. Four-dimensional z-stacks of 5–10 µm at 0.5 µm intervals were acquired every 2-3min. Movies were performed on the ventral side of the ventral nerve cord. Images were subsequently analysed and processed using Fiji (Schindelin, J. 2012).

Quantification of cortex glia nuclei and mitotic cortex glia

Wild-type brains expressing RFP or GFP-tagged (*Hist::RFP* or *Hist::YFP*, respectively) driven by *cyp4g15-GAL4*, were stained with phospho-histone H3 antibody to detect mitotic CG. Entire brains were imaged and quantification of total and mitotic CG nuclei numbers were performed in Volocity using adjusted protocols for detection of objects.

Cell cycle analysis (FUCCI)

We used the Fly-FUCCI system[39] that allows to discriminate between different phases of the cell cycle by expressing truncated forms of E2F and Cyclin B (CycB) fused to EGFP and mRFP1, respectively (EGFP::E2F 1-230, mRFP1::CycB 1-266). We used the *cyp4g15-GAL4* driver to express UAS-EGFP::E2F 1-230 and UAS-mRFP1::CycB 1-266 in CG cells. Staging of larvae was performed at 25°C and brains were dissected in PBS at ALH0, ALH24, ALH48, ALH72 and ALH96. Brains where immediately fixed in 4 % formaldehide diluted in PBS for 20 min, washed 3 times in PBS and mounted in Mowiol mounting medium on glass slides. Samples were imaged as described above and quantification of G1 (green), S (red) and G2/M CG nuclei was performed in Volocity.

Multicolour clonal analyses (Raeppli)

Heat-inducible Raeppli clones were generated by crossing *yw; UAS-Raeppli-CAAX 43E; cyp4g15-Gal4/TM6B* or *yw; UAS-Raeppli-nls 53D; cyp4g15-Gal4/TM6B* males to *hs-FLP* females. For knockdown experiments, chosen RNAi lines were crossed with *yw, hs-FLP; cyp-FRT-STOP-FRT-LexA/CyO; cyp4g15-GAL4, LexO-Raeppli-CAAX 43E*. Freshly hatched larvae (ALH0) were heat shocked for 2 hours at 37°C and aged to ALH24, ALH48,

ALH72 and ALH96 at 25°C, or at 29°C for RNAi experiments. For the visualization of clones at ALH0, constitutively expressed *Cyp-FLP* females were crossed to *yw; UAS-Raeppli-CAAX 43E; cyp4g15-Gal4/TM6B* males. Immunolabelling of NSCs for figure 1e was performed as described above. For all other experiments, CNS were dissected and fixed for 20 min in 4% formaldehyde in PBS and washed three times in PBS before mounting. Images were acquired as described above using the spectral mode of a Zeiss LSM880 confocal to promote fluorophore separation.

Quantification of clone volumes (Raeppli)

Raeppli TFP1 clones were chosen for quantification as it is the strongest and sharpest of the four Raeppli fluorophores. Only clones in the ventral nerve cord were measured. Volumes were measured in 3D images using Volocity 6.3 (Quorum technologies).

Quantification of clone overlap (Raeppli)

Z stacks of Raeppli CAAX 53E clones induced in CG were visualized in Icy v2.1.4.0 (Institut Pasteur and France Bioimaging, license GPLv3). Boundaries of all one-colour clones, for each of the 4 possible, were mapped manually and outlined with polygons. The same was done in the rare case of full colour overlap. Partial overlaps between clones (defined as an overlap between the colours of adjacent clones that do not cover fully any of the two clones) were then counted manually, with their position recorded on the stack by drawing an ellipse. The clones were counted in the VNC only, stopping at the middle of the neuropile coming from the ventral side, as the great majority of NSCs are located ventrally.

The number of overlaps counted corresponds to the number of fusion events, that we then divided by the total number of clones to generate a “Number of events/clones”.

Clonal analyses using CoinFLP

The recently described Coin-FLP method[57] was used to generate red and green mosaics of CG cells. CoinFLP clones were generated by crossing *Cyp-FLP; CoinFLP* females to *yw; LexAop-mCherry; UAS-GFP* or *yw; LexAop-mCherry-mito; UAS-mito-GFP* males and maintained at 25°C. Larvae were staged to ALH48-ALH72 at 25°C. For fixed tissue analyses, brains were dissected and fixed for 20 min in 4% formaldehyde in PBS and washed three times in PBS before mounting. Images were acquired as described above. For live imaging and FLIP experiments (see below), CNS were dissected in Schneider’s medium and mounted as described for live imaging.

147 **Fluorescence loss in photobleaching (FLIP)**

148 FLIP experiments were performed in dissected larval brains mounted as described above
149 for live imaging. Fluorescence in a selected region of interest (ROI) within a CG cell was
150 repeatedly photobleached over time, and loss of fluorescence in nonbleached regions were
151 monitored. Bleaching was performed on GFP expressed in CG using the *cyp4g15-GAL4*
152 driver. Laser line 488 was used at 100%. Images were acquired as follows: one z-stack of
153 5–10 µm at 0.3-0.5 µm intervals before bleaching (Pre-bleach), followed by 100 continuous
154 acquisitions at the bleaching plane during the bleaching (Bleach) and one z-stack of 5–
155 10 µm at 0.3-0.5 µm intervals after bleaching (Post-bleach). Images were subsequently
156 analysed and processed using Fiji.

157

158 **Quantitative analysis of ploidy by fluorescence in situ hybridization (FISH) of**
159 **chromosomes**

160 The FISH protocol was performed as previously described (Gogendeau et al., 2015) using
161 oligonucleotide probes for chromosomes II and III labelled with 5′CY3 and FAM488
162 fluorescent dyes respectively (gift from R. Basto). FISH was performed in CNS expressing
163 Histone::RFP or Histone::GFP in CG and dissected in PBS at ALH0, ALH24, ALH48, ALH72
164 and ALH96. Briefly, dissected brains were fixed for 30 min in 4% formaldehyde prepared in
165 PBS with 0.1% tween 20, washed three times/ 10min in PBS, washed once 10min in
166 2xSSCT (2xSSC (Sigma S6639) + 0.1% tween-20) and once in 2xSSCT 50% formamide
167 (Sigma 47671). For the pre-hybridization step, CNS were transfered to a new tube
168 containing 2xSSCT 50% formamide pre-warmed at 92°C and denatured 3min at 92°C. For
169 the hybridization step, the DNA probe (40-80 ng) was prepared in hybridization buffer (20%
170 dextran sulphate, 2XSSCT, 50% deionized formamide (Sigma F9037), 0.5 mg ml−1 salmon
171 sperm DNA) and denatured 3min at 92°C. Probes were added to the brains samples and
172 hybridize 5min at 92°C followed by overnight hybridization at 37°C. Samples were washed
173 with 60°C pre-warmed 2XSSCT for 10 min, washed once 5min in 2XSSCT at RT and rinsed
174 in PBS. CNS were mounted in Mowiol mounting medium and imaged as described above.
175 FISH signals for chromosomes II and III were quantified in randomly selected CG nuclei
176 using adapted protocols for dots inside objects detection in 3D images in Volocity.

177

178 **Statistics and reproducibility**

179 Statistical tests used for each experiment are stated in the figure legends. Statistical tests
180 were performed using GraphPad Prism 7.0a.

181

Acknowledgments

We thank the Abmayr and Workman labs for the generous gift of the anti-Mbc and anti-Kirre antibodies; the Basto lab for the DNA FISH probes and the rabbit anti-Dpn; Steven Stowers and Matthias Landgraf for sharing plasmids for Multisite Gateway cloning; M'hamed Khalil Mazouni for the sequence of the FRT-STOP-FRT cassette; the Freeman lab for alrm-GAL4; James Skeath for the Dpn plasmid; the Bloomington Drosophila Stock Center and the Vienna Drosophila Research Center for RNAi lines. We are grateful to Mateusz Trylinski for help with Fiji scripts and discussions for ploidy count. Julie Marc generated part of Figure 1e. Laurence Arbogast built the *cyp4g15-FLP* and *cyp4g15-FRT-STOP-FRT-LexA* constructs. We thank Romain Levayer for critical reading of the manuscript.

This work has been funded by a starting package from Institut Pasteur/LabEx Revive, a JCJC grant from Agence Nationale de la Recherche (NeuraSteNic, ANR- 17-CE13-0010-01) and a Projet Fondation ARC from Fondation ARC pour la Recherche sur le Cancer to PS. MAR has been supported by a LabEx Revive postdoctoral fellowship.

Author Contributions

MAR performed all experiments, except for: Figure 5a-c and Figure 3e performed by DB; Figure 3c-d, and Supp. Figure S1d-e performed by BD under the supervision of MAR; and parts of Figures 1e, 5 and 6 performed by PS. MAR, BD and PS quantified and analysed the data. MAR and PS wrote the article and MAR made the figures.

Declaration of Interests

The authors declare no competing interest.

Data availability statement

The datasets generated during and/or analysed during the current study are available from the corresponding author on reasonable request.

REFERENCES

1. Paridaen, J. T. M. L. & Huttner, W. B. Neurogenesis during development of the vertebrate central nervous system. **15**, 351–364 (2014).

2. Bond, A. M., Ming, G. L. & Song, H. Adult Mammalian Neural Stem Cells and Neurogenesis: Five Decades Later. *Cell Stem Cell* **17**, 385–395 (2015).

3. Götz, M., Nakafuku, M. & Petrik, D. Neurogenesis in the developing and adult brain—similarities and key differences. *Cold Spring Harb. Perspect. Biol.* **8**, (2016).

4. Martynoga, B. *et al.* Epigenomic enhancer annotation reveals a key role for NFIX in neural stem cell quiescence. *Genes Dev.* **27**, 1769–1786 (2013).

5. Faigle, R. & Song, H. Signaling mechanisms regulating adult neural stem cells and neurogenesis. *Biochim. Biophys. Acta* **1830**, 2435–48 (2013).

6. Stricker, S. H. & Götz, M. DNA-methylation: Master or slave of neural fate decisions? *Frontiers in Neuroscience* **12**, (2018).

7. Morante-Redolat, J. M. & Porlan, E. Neural Stem Cell Regulation by Adhesion Molecules Within the Subependymal Niche. (2019). doi:10.3389/fcell.2019.00102

8. Bjornsson, C. S., Apostolopoulou, M., Tian, Y. & Temple, S. It Takes a Village: Constructing the Neurogenic Niche. *Dev. Cell* **32**, 435–446 (2015).

9. Silva-Vargas, V., Crouch, E. E. & Doetsch, F. Adult neural stem cells and their niche: A dynamic duo during homeostasis, regeneration, and aging. *Curr. Opin. Neurobiol.* **23**, 935–942 (2013).

10. Conover, J. C. & Todd, K. L. *Neuronal Stem Cell Niches of the Brain*. *Biology and Engineering of Stem Cell Niches* (2017). doi:10.1016/B978-0-12-802734-9.00006-8

11. Obernier, K. & Alvarez-Buylla, A. Neural stem cells: Origin, heterogeneity and regulation in the adult mammalian brain. *Development (Cambridge)* **146**, (2019).

12. Lacar, B., Young, S. Z., Platel, J.-C. & Bordey, A. Gap junction-mediated calcium waves define communication networks among murine postnatal neural progenitor cells. *Eur. J. Neurosci.* **34**, 1895–905 (2011).

13. Platel, J. C. & Bordey, A. The multifaceted subventricular zone astrocyte: From a metabolic and pro-neurogenic role to acting as a neural stem cell. *Neuroscience* **323**, 20–28 (2016).

14. Conover, J. C. & Todd, K. L. Development and aging of a brain neural stem cell niche. *Exp. Gerontol.* **94**, 9–13 (2017).

15. Homem, C. C. F. & Knoblich, J. a. Drosophila neuroblasts: a model for stem cell biology. *Development* **139**, 4297–310 (2012).

16. Mira, H. & Morante, J. Neurogenesis From Embryo to Adult – Lessons From Flies and Mice. *Frontiers in Cell and Developmental Biology* **8**, 533 (2020).

17. Egger, B., Chell, J. M. & Brand, A. H. Insights into neural stem cell biology from flies. *Philos Trans R Soc L. B Biol Sci* **363**, 39–56 (2008).

18. Otsuki, L. & Brand, A. H. Cell cycle heterogeneity directs the timing of neural stem

cell activation from quiescence. *Science* **360**, 99–102 (2018).

19. Britton, J. S. & Edgar, B. A. Environmental control of the cell cycle in Drosophila: nutrition activates mitotic and endoreplicative cells by distinct mechanisms. *Development* **125**, 2149–2158 (1998).

20. Truman, J. W. & Bate, M. Spatial and temporal patterns of neurogenesis in the central nervous system of Drosophila melanogaster. *Dev. Biol.* **125**, 145–157 (1988).

21. Chell, J. M. & Brand, A. H. Nutrition-responsive glia control exit of neural stem cells from quiescence. *Cell* **143**, 1161–73 (2010).

22. Sousa-Nunes, R., Yee, L. L. & Gould, A. P. Fat cells reactivate quiescent neuroblasts via TOR and glial insulin relays in Drosophila. *Nature* **471**, 508–12 (2011).

23. Spéder, P. & Brand, A. H. Gap Junction Proteins in the Blood-Brain Barrier Control Nutrient-Dependent Reactivation of Drosophila Neural Stem Cells. *Dev. Cell* 309–321 (2014). doi:10.1016/j.devcel.2014.05.021

24. Dumstrei, K., Wang, F. & Hartenstein, V. Role of DE-cadherin in neuroblast proliferation, neural morphogenesis, and axon tract formation in Drosophila larval brain development. *J. Neurosci.* **23**, 3325–35 (2003).

25. Pereanu, W., Shy, D. & Hartenstein, V. Morphogenesis and proliferation of the larval brain glia in Drosophila. *Dev. Biol.* **283**, 191–203 (2005).

26. Spéder, P. & Brand, A. H. Systemic and local cues drive neural stem cell niche remodelling during neurogenesis in Drosophila. *Elife* **7**, 1–16 (2018).

27. Bailey, A. P. *et al.* Antioxidant Role for Lipid Droplets in a Stem Cell Niche of Drosophila. *Cell* **163**, 340–353 (2015).

28. Cheng, L. Y. *et al.* Anaplastic lymphoma kinase spares organ growth during nutrient restriction in Drosophila. *Cell* **146**, 435–47 (2011).

29. Coutinho-Budd, J. C., Sheehan, A. E. & Freeman, M. R. The secreted neurotrophin spätzle 3 promotes glial morphogenesis and supports neuronal survival and function. *Genes Dev.* **31**, 2023–2038 (2017).

30. Read, R. D. Pvr receptor tyrosine kinase signaling promotes post-embryonic morphogenesis, and survival of glia and neural progenitor cells in drosophila. *Dev.* **145**, (2018).

31. Plazaola-Sasieta, H. *et al.* Drosophila ClC-a is required in glia of the stem cell niche for proper neurogenesis and wiring of neural circuits. *Glia* **67**, 2374–2398 (2019).

32. Yuan, X., Sipe, C. W., Suzawa, M., Bland, M. L. & Siegrist, S. E. Dilp-2-mediated PI3-kinase activation coordinates reactivation of quiescent neuroblasts with growth of their glial stem cell niche. *PLoS Biol.* **18**, (2020).

33. Kiyoshi, C. & Zhou, M. Astrocyte syncytium: a functional reticular system in the brain. *Neural Regen. Res.* **14**, 595 (2019).

34. Kanca, O., Caussinus, E., Denes, A. S., Percival-Smith, A. & Affolter, M. Raeppli: a whole-tissue labeling tool for live imaging of Drosophila development. *Development*

141, 472–480 (2014).

35. Fox, D. T. & Duronio, R. J. Endoreplication and polyploidy: insights into development and disease. *Development* **140**, 3–12 (2013).

36. Edgar, B. A., Zielke, N. & Gutierrez, C. Endocycles : a recurrent evolutionary innovation for post-mitotic cell growth. (2014). doi:10.1038/nrm3756

37. Orr-Weaver, T. L. When bigger is better: The role of polyploidy in organogenesis. *Trends Genet.* **31**, 307–315 (2015).

38. Avet-Rochex, A., Kaul, A. K., Gatt, A. P., McNeill, H. & Bateman, J. M. Concerted control of gliogenesis by InR/TOR and FGF signalling in the Drosophila post-embryonic brain. *Development* **139**, 2763–72 (2012).

39. Zielke, N. *et al.* Fly-FUCCI: A Versatile Tool for Studying Cell Proliferation in Complex Tissues. *Cell Rep.* **7**, 588–598 (2014).

40. Piekny, A. J. & Maddox, A. S. The myriad roles of Anillin during cytokinesis. *Seminars in Cell and Developmental Biology* **21**, 881–891 (2010).

41. Hu, C. K., Coughlin, M. & Mitchison, T. J. Midbody assembly and its regulation during cytokinesis. *Mol. Biol. Cell* **23**, 1024–1034 (2012).

42. Gogendeau, D. *et al.* Aneuploidy causes premature differentiation of neural and intestinal stem cells. *Nat. Commun.* **6**, 1–15 (2015).

43. Unhavaithaya, Y. & Orr-Weaver, T. L. Polyploidization of glia in neural development links tissue growth to blood-brain barrier integrity. *Genes Dev.* **26**, 31–6 (2012).

44. Hong, A. *et al.* The cyclin-dependent kinase inhibitor Dacapo promotes replication licensing during Drosophila endocycles. *EMBO J.* **26**, 2071–2082 (2007).

45. Frawley, L. E. & Orr-Weaver, T. L. Polyploidy. *Current Biology* **25**, R353–R358 (2015).

46. Øvrebø, J. I. & Edgar, B. A. Polyploidy in tissue homeostasis and regeneration. *Development (Cambridge)* **145**, (2018).

47. Lippincott-Schwartz, J., Altan-Bonnet, N. & Patterson, G. H. Photobleaching and photoactivation: Following protein dynamics in living cells. *Nat. Rev. Mol. Cell Biol.* **4**, 6–14 (2003).

48. Miyawaki, A. Proteins on the move: Insights gained from fluorescent protein technologies. *Nat. Rev. Mol. Cell Biol.* **12**, 656–668 (2011).

49. Peterman, E. & Prekeris, R. The postmitotic midbody: Regulating polarity, stemness, and proliferation. *Journal of Cell Biology* **218**, 3903–3911 (2019).

50. Dittmar, T. & Zänker, K. S. Cell Fusion in Health and Disease. I Cell Fusion in Health. in *Advances in Experimental Medicine and Biology* (eds. Dittmar, T. & Zänker, K. S.) **713**, (Springer-Verlag, Berlin, Germany, 2011).

51. Dittmar, T. & Zänker, K. S. Cell Fusion in Health and Disease. II Cell Fusion in Disease. in *Advances in Experimental Medicine and Biology* (eds. Dittmar, T. & Zänker, K. S.) (Springer-Verlag, Berlin, Germany, 2011).

52. Bastida-Ruiz, D., Van Hoesen, K. & Cohen, M. The dark side of cell fusion. *International Journal of Molecular Sciences* **17**, (2016).

53. Zito, F., Lampiasi, N., Kireev, I. & Russo, R. United we stand: Adhesion and molecular mechanisms driving cell fusion across species. *European Journal of Cell Biology* **95**, 552–562 (2016).

54. Brukman, N. G., Uygur, B., Podbilewicz, B. & Chernomordik, L. V. How cells fuse. *Journal of Cell Biology* **218**, 1436–1451 (2019).

55. Hernández, J. M. & Podbilewicz, B. The hallmarks of cell-cell fusion. *Development* **144**, 4481–4495 (2017).

56. Kim, J. H. & Chen, E. H. The fusogenic synapse at a glance. *Journal of cell science* **132**, (2019).

57. Bosch, J. A., Tran, N. H. & Hariharan, I. K. CoinFLP: a system for efficient mosaic screening and for visualizing clonal boundaries in Drosophila. *Development* **142**, 597–606 (2015).

58. Abmayr, S. M. & Pavlath, G. K. Myoblast fusion: Lessons from flies and mice. *Development* **139**, 641–656 (2012).

59. Deng, S., Azevedo, M. & Baylies, M. Acting on identity: Myoblast fusion and the formation of the syncytial muscle fiber. *Seminars in Cell and Developmental Biology* **72**, 45–55 (2017).

60. Lee, D. M. & Chen, E. H. Drosophila Myoblast Fusion: Invasion and Resistance for the Ultimate Union. *Annual Review of Genetics* **53**, 67–91 (2019).

61. Haralalka, S. *et al.* Asymmetric Mbc, active Rac1 and F-actin foci in the fusioncompetent myoblasts during myoblast fusion in Drosophila. *Development* **138**, 1551–1562 (2011).

62. Venken, K. J. T. *et al.* MiMIC: A highly versatile transposon insertion resource for engineering Drosophila melanogaster genes. *Nat. Methods* **8**, 737–747 (2011).

63. Nagarkar-Jaiswal, S. *et al.* A library of MiMICs allows tagging of genes and reversible, spatial and temporal knockdown of proteins in Drosophila. *Elife* **2015**, 1–28 (2015).

64. Bosch, J. A., Sumabat, T. M. & Hariharan, I. K. Persistence of RNAi-mediated knockdown in Drosophila complicates mosaic analysis yet enables highly sensitive lineage tracing. *Genetics* **203**, 109–118 (2016).

65. Evans, C. J. *et al.* G-TRACE: Rapid Gal4-based cell lineage analysis in Drosophila. *Nat. Methods* **6**, 603–605 (2009).

66. Zielke, N., Edgar, B. A. & DePamphilis, M. L. Endoreplication. *Cold Spring Harbor Perspectives in Biology* **5**, (2013).

67. Greenbaum, M. P., Iwamori, T., Buchold, G. M. & Matzuk, M. M. Germ cell intercellular bridges. *Cold Spring Harb. Perspect. Biol.* **3**, 1–18 (2011).

68. Huynh, J.-R. Fusome as a Cell-Cell Communication Channel of Drosophila Ovarian Cyst. (2013).

69. Willkomm, L. & Bloch, W. State of the art in cell-cell fusion. in *Cell Fusion: Overviews and Methods: Second Edition* **1313**, 1–19 (Springer New York, 2015).

70. Acquistapace, A. *et al.* Human mesenchymal stem cells reprogram adult cardiomyocytes toward a progenitor-like state through partial cell fusion and mitochondria transfer. *Stem Cells* **29**, 812–824 (2011).

71. Ljubojevic, N., Henderson, J. M. & Zurzolo, C. The Ways of Actin: Why Tunneling Nanotubes Are Unique Cell Protrusions. *Trends in Cell Biology* **31**, 130–142 (2021).

72. Cordero Cervantes, D. & Zurzolo, C. Peering into tunneling nanotubes-The path forward. *EMBO J.* e105789 (2021). doi:10.15252/embj.2020105789

73. Peterson, N. G. *et al.* Cytoplasmic sharing through apical membrane remodeling. *Elife* **9**, 1–50 (2020).

74. Van De Peer, Y., Mizrachi, E. & Marchal, K. The evolutionary significance of polyploidy. *Nature Reviews Genetics* **18**, 411–424 (2017).

75. Giaume, C., Koulakoff, A., Roux, L., Holcman, D. & Rouach, N. Astroglial networks: a step further in neuroglial and gliovascular interactions. *Nat. Rev. Neurosci.* **11**, 87–99 (2010).

76. Kiyoshi, C. M. & Zhou, M. Astrocyte syncytium: A functional reticular system in the brain. *Neural Regeneration Research* **14**, 595–596 (2019).

77. Dias, M. C., Mapunda, J. A., Vladymyrov, M. & Engelhardt, B. Structure and junctional complexes of endothelial, epithelial and glial brain barriers. *International Journal of Molecular Sciences* **20**, 5372 (2019).

78. Giordano-Santini, R., Linton, C. & Hilliard, M. A. Cell-cell fusion in the nervous system: Alternative mechanisms of development, injury, and repair. *Seminars in Cell and Developmental Biology* **60**, 146–154 (2016).

79. Korenkova, O., Pepe, A. & Zurzolo, C. Fine intercellular connections in development: TNTs, cytonemes, or intercellular bridges? *Cell Stress* **4**, 30–43 (2020).

80. Doherty, J., Logan, M. a, Taşdemir, O. E. & Freeman, M. R. Ensheathing glia function as phagocytes in the adult Drosophila brain. *J. Neurosci.* **29**, 4768–81 (2009).

81. Bellaïche, Y., Gho, M., Kaltschmidt, J. A., Brand, A. H. & Schweisguth, F. Frizzled regulates localization of cell-fate determinants and mitotic spindle rotation during asymmetric cell division. *Nat. Cell Biol.* **3**, 50–57 (2001).

82. Langevin, J. *et al.* Lethal giant larvae controls the localization of Notch-signaling regulators Numb, neuralized, and Sanpodo in Drosophila sensory-organ precursor cells. *Curr. Biol.* **15**, 955–962 (2005).

83. Pfeiffer, B. D. *et al.* Tools for neuroanatomy and neurogenetics in Drosophila. *Proc. Natl. Acad. Sci. U. S. A.* **105**, 9715–20 (2008).

84. Böttcher, R. *et al.* Efficient chromosomal gene modification with CRISPR/cas9 and PCR-based homologous recombination donors in cultured Drosophila cells. *Nucleic Acids Res.* **42**, (2014).

85. Petersen, L. K. & Stowers, R. S. A Gateway MultiSite recombination cloning toolkit. *PLoS One* **6**, e24531 (2011).

Figure legends Rujano et al.

Figure 1: Growth of individual CG cells results in a tiled organization of the cortex glia network

a) Schematic of the Drosophila NSC niche depicting the blood brain barrier (BBB), which is made by the perineurial glia (PG, red) and subperineurial glia (SPG, orange), the cortex glia (CG, green), neural stem cells (NSC, grey), ganglion mother cells/intermediate progenitors (gmc/inp, blue) and neurons (N, magenta).

b) Ventral region in the larval ventral nerve cord (VNC) at ALH72 (at 25°C) labelled with markers for the CG membranes (*Nrv2::GFP*, green), CG nuclei (*CG* > *Hist::RFP*, yellow), NSC (anti-Dpn, grey) and neurons (anti-ELAV, magenta). The right panel shows the CG membrane separately. Scale bar: 10 μm.

c) Timeline of neurogenesis (top scheme) and assessment of CG network organization during larval development in the entire CNS at ALH0, ALH24, ALH48, ALH72 and ALH96 (at 25°C). Two main neurogenic regions are the central brain (CB), comprising two hemispheres, and the ventral nerve cord (VNC). CG membranes are labelled with *Nrv2::GFP* (ALH0, ALH72) and *CG>CD8::GFP* (ALH24, ALH48 and ALH96). Scale bar: 50 μm.

d) Progressive growth and adaptation of the CG network to NSC lineages in the VNC visualized at ALH0, ALH24, ALH48, ALH72 and ALH96 (at 25°C). CG membranes are labelled with *CG>CD8::GFP* (ALH0) and *Nrv2::GFP* (ALH24, ALH48, ALH72 and ALH96). NSCs are labelled with Dpn (grey). Scale bars: 20 μm.

e) Analysis of individual CG growth over time by multicolour lineage tracing using Raeppli. Images were acquired at ALH0, ALH24, ALH48, ALH72 and ALH96 (at 25°C). Constitutively expressed Cyp-Flp was used for the visualization of clones at ALH0. Hs-Flp and heat shock induction at 37°C at ALH0 was used for the visualization of clones at ALH24, ALH48, ALH72 and ALH96. Scale bars: 20 μm.

f) Volume quantification of Raeppli clones in the VNC at ALH0 (n=7), ALH24 (n=25), ALH48 (n=25), ALH72 (n=32) and ALH96 (n=30). n, number of clones. Results are presented as box and whisker plots. Whiskers mark the minimum and maximum, the box includes the 25th–75th percentile, and the line in the box is the median. Individual values are superimposed. Data statistics: ordinary one-way ANOVA with a Tukey's multiple comparison test.

g) Individual TagBFP (cyan) and E2-orange (yellow) Raeppli clones encasing several NSC labelled with Dpn (magenta). Scale bar: 20 μm.

h) Number of NSCs per CG clone quantification in the central brain (CB) and the VNC at ALH48 (n=53 and 51 CB and VNC, respectively), ALH72 (n=64 and 48 CB and VNC, respectively) and ALH96 (n=46 and 42 CB and VNC, respectively). n, number of clones. Bars represent the mean and the error bars are the standard deviation. Data statistics: two-way ANOVA with a Dunnett's multiple comparison test.

Figure 2: CG cells exhibit multiple cell cycle strategies

a) G1 (green), S (magenta) and G2/M (grey) phases of the cell cycle along CG network detected with Fly-FUCCI. FUCCI sensors are labelled in magenta (CycB) and green (E2F1). Scale bar: 50 μm.

b) Quantification of cell cycle phase distribution in CG by Fly-FUCCI at ALH0 (n=11), ALH24 (n=15), ALH48 (n=23), ALH72 (n=13) and ALH96 (n=6) (at 25°C). n, number of CNS analysed. Stacked bars represent the percentage of cells in each phase.

c) Representative image of a larval VNC expressing Hist::RFP in CG (magenta) and stained with phospho-histone H3 antibody (pHistone-3, green) to visualise mitotic CG nuclei (grey). Scale bar: 20 μm. Higher magnification of separate channels from the region inside the dashed rectangle are shown on the right.

d) CG mitotic index quantification in larval CNS at ALH0 (n=15), ALH24 (n=26), ALH48 (n=27), ALH72 (n=13) and ALH96 (n=13) (at 25°C). n, number of CNS analysed. Results are presented as box and whisker plots. Whiskers mark the minimum and maximum, the box includes the 25th–75th percentile, and the line in the box is the median. Individual values are superimposed. Data statistics: ordinary one-way ANOVA with a Tukey's multiple comparison test.

e) Still images of a time-lapse movie (Movie S1) of mitotic CG expressing *Hist::RFP* (grey). Scale bar: 5 μm.

f) Expression of *mRFP::scra* (magenta) in CG to monitor contractile ring and midbody formation. CG membranes and nuclei are labelled with *Nrv2::GFP* (green) and *Hist::IFP* (blue) respectively. Arrows indicate midbodies/contractile ring. Scale bar: 10 μm. Higher magnifications of *mRFP::scra* and *Nrv2::GFP* separate channels from the region demarcated by the dashed rectangle are shown on the right.

g) Quantification of the number of midbodies per 100 CG cells in larval VNCs at ALH24 (n=4), ALH48 (n=8), ALH72 (n=4) and ALH96 (n=4) (at 25°C). n, number of VNCs analysed.

Results are presented as box and whisker plots. Whiskers mark the minimum and maximum, the box includes the 25th–75th percentile, and the line in the box is the median. Individual values are superimposed. Data statistics: ordinary one-way ANOVA with a Tukey's multiple comparison test.

h) Fluorescence in situ hybridization (FISH) using probes for chromosomes 2 (Chr2, cyan) and 3 (Chr3, red) in CNS expressing nls::LacZ (yellow) to mark the CG nuclei. 2n (upper) and >2n (bottom) nuclei are shown. Scale bar: 5 μm.

i) Quantification of FISH signals in CG nuclei at ALH0 (n=95), ALH24 (n=189), ALH48 (n=140), ALH72 (n=70) and ALH96 (n=108). N, number of CG cells analysed. Results are presented as box and whisker plots. Whiskers mark the minimum and maximum, the box includes the 25th–75th percentile, and the line in the box is the median. Individual values are superimposed. Data statistics: two-way ANOVA with a Dunnett's multiple comparison test.

j, k) CG nuclei (j, *CG > Hist::RFP*) and CG network (k, *Nrv2::GFP*) in control CNS and in CNS where CG-specific downregulation of doubled-parked (*dup RNAi*) was induced. Scale bar: 20 μm.

l) Still images of a time-lapse movie (Movie S3) of a CG expressing *Hist::RFP* (grey) undergoing endomitosis. Scale bar: 5 μm.

Figure 3: CG glia are syncytial units

a) Still images of a time-lapse movie (Movie S4) of two CG expressing *Hist::RFP* (grey) undergoing mitosis synchronously. Scale bar: 5 μm.

b) Synchronous behaviour of CG observed with Fly-FUCCI (left panels), where clusters of CG are found at the same cell cycle phase, and with anillin staining that also show clusters of CG undergoing mitosis (*) and cytokinesis (**) at the same time (right panels). Synchronous clusters are delineated with dashed lines. FUCCI sensors are labelled in magenta (CycB) and green (E2F1). Anillin is labelled with mRFP::scra (magenta) and CG nuclei with Hist::IFP (blue). Separate channels are shown in the bottom. Scale bars: 20 μm.

c) Sharing of cytoplasmic material between CG assessed by Fluorescence Loss In Photobleaching (FLIP) of cytosolic GFP (green). Top panels depict a region in the VNC before (pre-bleach) and after bleaching (post-bleach). CG nuclei are labelled with *Hist::RFP* (magenta). Bottom panels show intermediate time points (GFP only, pseudocolored with thermal LUT) during continuous photobleaching. Bleached area is delineated by the dashed square. Scale bars: 20 μm.

d) Quantification of the number of CG nuclei in the bleached region after FLIP at ALH24 (n=23), ALH48 (n=16), ALH72 (n=8) and ALH96 (n=8). n, number of FLIP experiments analysed. Results are presented as box and whisker plots. Whiskers mark the minimum and maximum, the box includes the 25th–75th percentile, and the line in the box is the median. Individual values are superimposed. Data statistics: two-way ANOVA with a Dunnett's multiple comparison test.

e) CG connection via the midbodies marked by anillin (mRFP::scra, magenta) assessed by FLIP of cytosolic GFP (green). Top panels depict a region in the VNC before (pre-bleach) and after bleaching (post-bleach). CG nuclei are labelled with *Hist::RFP* (magenta). The bleached area delineated by the white dashed square is placed close to an isolated midbody (clear blue inset) in between CG cells. Bottom panels show intermediate time points (GFP only, pseudocolored with thermal LUT) during continuous photobleaching. Scale bars: 10 μm.

Figure 4: CG units can undergo cellular fusion

a) Restricted areas of colour overlapping in membrane targeted CG Raeppli clones at ALH72 (dashed lines). Scale bar: 50 μm.

b) Cytoplasmic exchange between CG units assessed in CoinFLP clones (methods and Supp. Fig. S4c). Clones expressing either cytosolic GFP (green) or cytosolic RFP (magenta), show regions of partial overlapping (dashed lines). Scale bar: 20 μm.

c) Quantification of areas of partial (grey-hashed green), total (grey) or no overlap (green) between clones expressing cytosolic GFP and RFP. Due to the bias in the CoinFLP system that generates very large connected clones in one colour (RFP in our case) and small sparse clones in the other colour (GFP), only green clones were taken in account for the no overlap category. Stacked bars represent the mean and error bars represent the SEM. Data statistics: two-way ANOVA with a Šídák's multiple comparisons test. No statistically significative differences were found.

d) Propagation of information/signals between fused areas was assessed by FLIP in clones generated by CoinFLP with cytosolic GFP (green) and RFP (magenta) in CG. A GFP expressing clone with areas of partial and no overlap with an RFP expressing clone was selected. Continuous bleaching was performed in a small area (dashed rectangle) of the non-overlapping zone, and loss of fluorescence was assessed in the overlapping area (grey, delineated by a dashed line). Top panels depict the assessed area before (pre-bleach) and

after bleaching (post-bleach). Bottom panels show intermediate time points (GFP only, pseudocolored with thermal LUT) during continuous photobleaching. Scale bars: 10 μm.

e) Continuity between CG units due to cellular fusion was assessed by FLIP of CG expressing cytosolic GFP in combination with early induction of multicolour labelling of CG nuclei (Raeppli-NLS) that leads to clonal labelling of the nuclei in CG units. Continuous bleaching was performed in a small area (dashed rectangle) containing nuclei of one colour. Top panels depict the assessed area before (pre-bleach) and after bleaching (post-bleach). Bottom panels show intermediate time points (GFP only, pseudocolored with thermal LUT) during continuous photobleaching. Scale bars: 20 μm.

f) Still images of a time-lapse movie (Movie S5) of the region of interaction between two neighbouring CG clones generated with CoinFLP and expressing either cytosolic GFP or RFP. Scale bar: 5 μm.

Figure 5: Cell fusion between CG units is regulated by canonical fusion molecules

a) Expression of membrane targeted GFP (*mCD8::GFP*, green) and nuclear RFP (*Hist::RFP*, magenta) using the trojan line *mbc-Gal4* to assess the expression of *mbc* in CG. Glia nuclei were labelled with Repo (blue) and NSC were labelled with Dpn (gray). Scale bar: 20 μm.

b) Endogenous expression of Mbc in the CNS assessed by immunostaining with Mbc antibody (magenta) in the VNC. CG membranes are labelled with *Nvr2::GFP* (green), NSC are labelled with Dpn (grey) and Dapi (blue) was used to visualise all nuclei. Upper panels show the expression in control CNS. Lower panels show the expression after RNAi knockdown of *mbc*. Scale bar: 10 μm.

c) Endogenous expression of Kirre in the CNS assessed by immunostaining with Kirre antibody (magenta) in the VNC. CG membranes are labelled with Nvr2::GFP (green), NSC are labelled with Dpn (grey) and Dapi (blue) was used to visualise all nuclei. Upper panels show the expression in control CNS. Lower panels show the expression after RNAi mediated down regulation of *kirre*. Scale bar: 10 μm.

d) RNAi knockdown of cell-cell fusion related genes in multicoloured labelled CG (Raeppli CAAX) in the VNC. Control (no RNAi), *WASp*, *mbc*, *hbs*, *rst* and *sns* RNAi-knockdowns are shown. RNAi expression was induced at ALH0, larvae were maintained at 29°C and dissected at ALH72. Scale bars: 50 μm.

e, f) Quantification of the number of fusion events per clone (e) and number of clones (f) for multicoloured labelled Raeppli CG clones at ALH72 (at 29°C) after knockdown of fusion

genes in CG. Results are presented as box and whisker plots. Whiskers mark the minimum and maximum, the box includes the 25th–75th percentile. Individual values are superimposed. Data statistics: one-way ANOVA with a Kruskal–Wallis multiple comparison test.

Figure 6: Cellular fusion of CG units is required for correct CG architecture

a) Effect of down regulation of cell-cell fusion genes on CG network architecture. RNAi knockdown of *WASp*, *mbc*, *dock*, *kirre* and *sns* at ALH72 (at 29°C) are shown. CG network architecture is visualised with Nrv2::GFP. Yellow arrows point towards noticeable defects in the network architecture. Scale bars: 10 μm.

b) Model of CG morphogenesis along developmental time and NSC behaviour. Individual CG cells grow to tile the CNS, undergoing both endoreplicative and mitotic events that create multinucleated and polyploid cells. These syncytial units are also able to fuse with each other, exchanging subcellular compartments including cytoplasm, membrane and organelles. This fusion appears partial and can lead to sharp boundaries between connected and unconnected CG domains, as illustrated by the dashed lines. Each CG unit is able to enwrap several NSC lineages. Polyploid nuclei are shown in darker blue.

Rujano et al. Figure 1

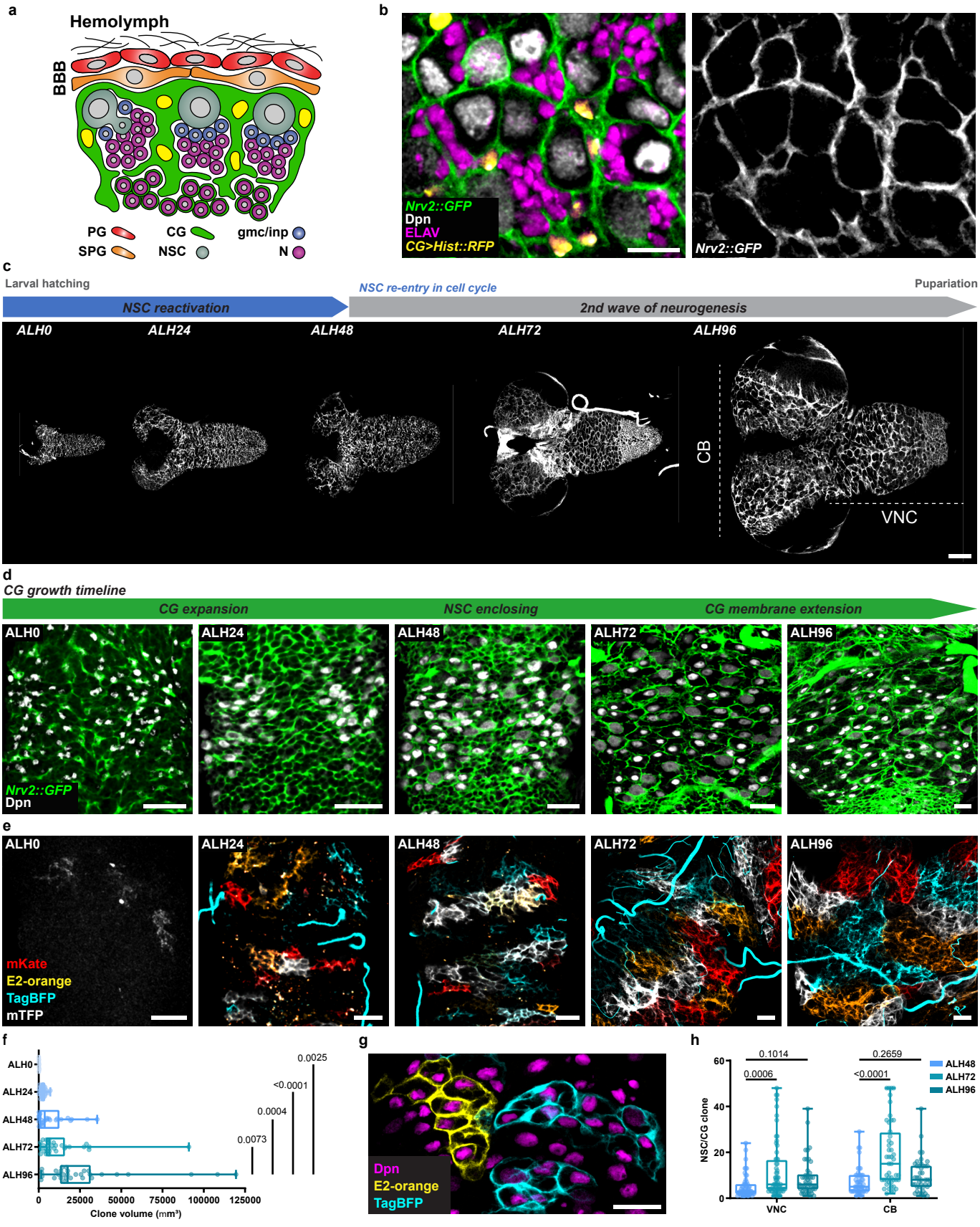

Rujano et al. Figure 2

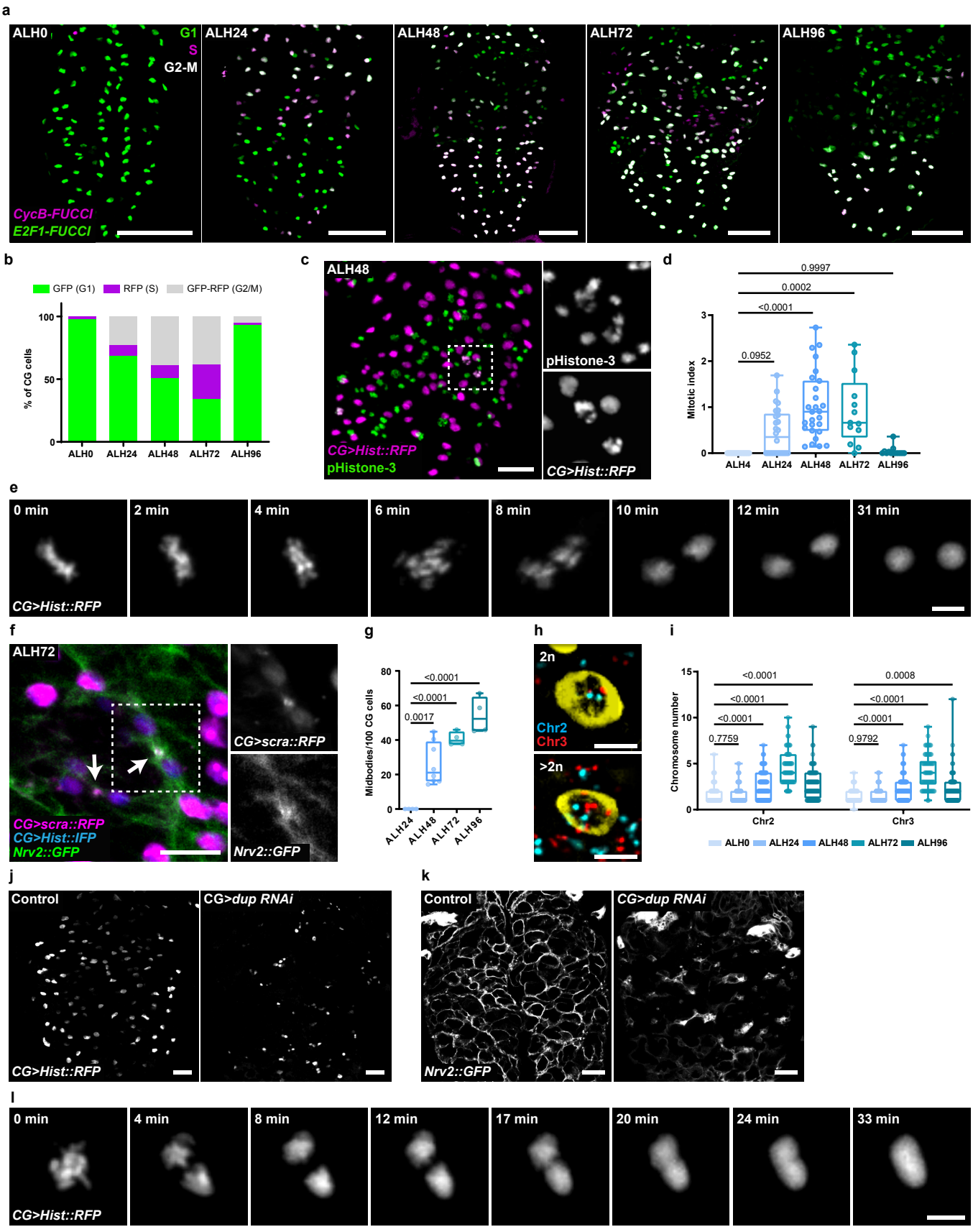

Rujano et al. Figure 3

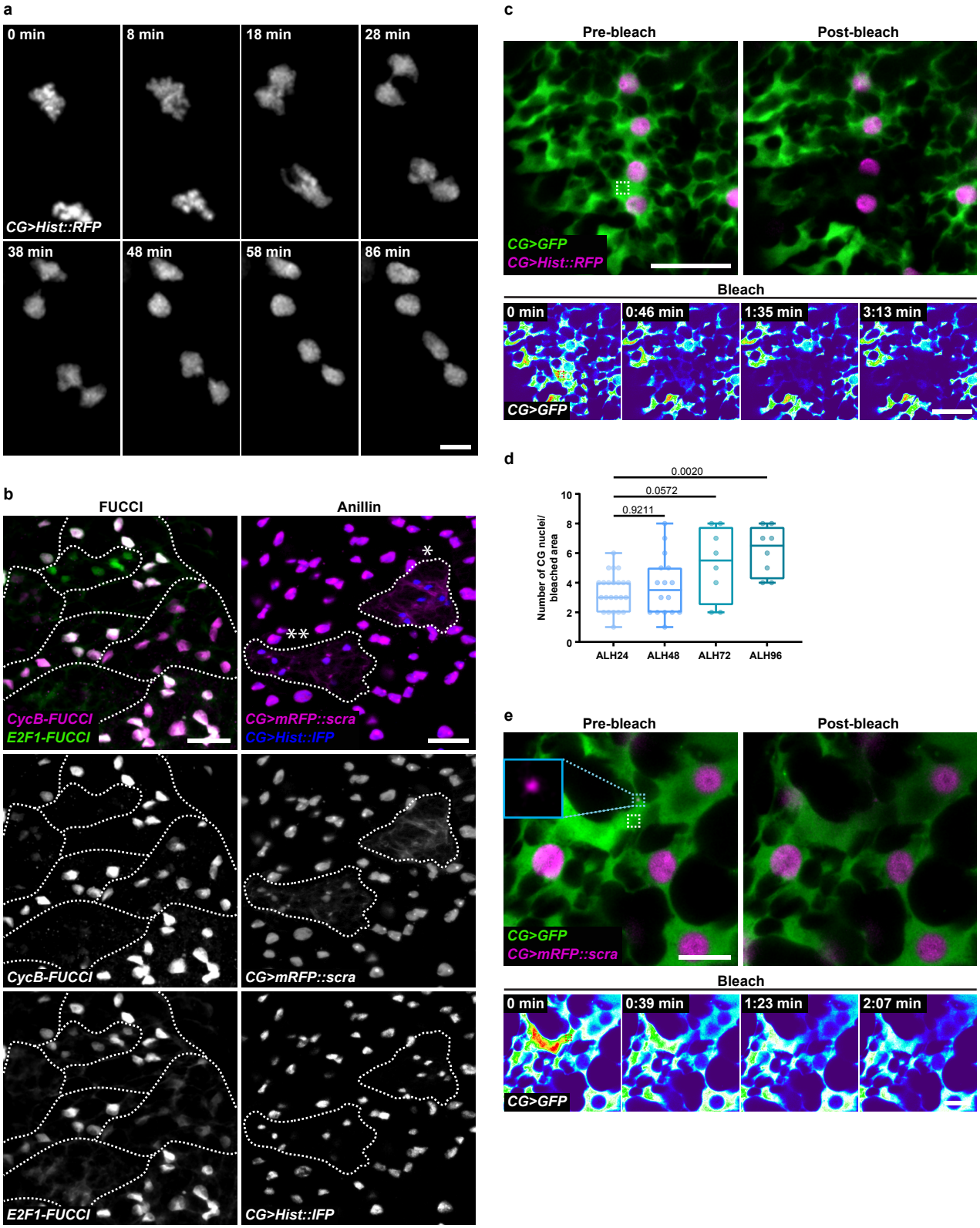

Rujano et al. Figure 4

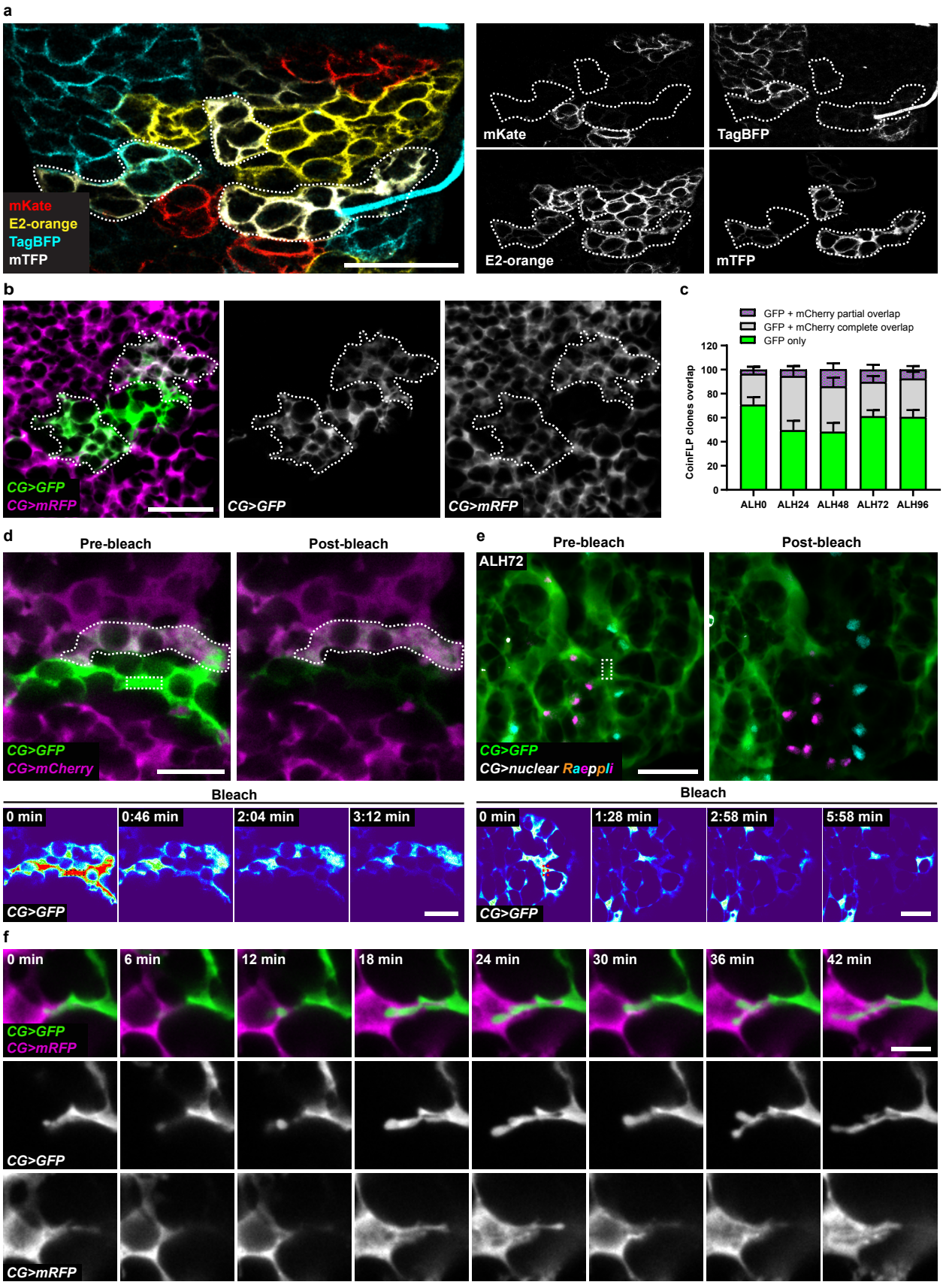

Rujano et al. Figure 5

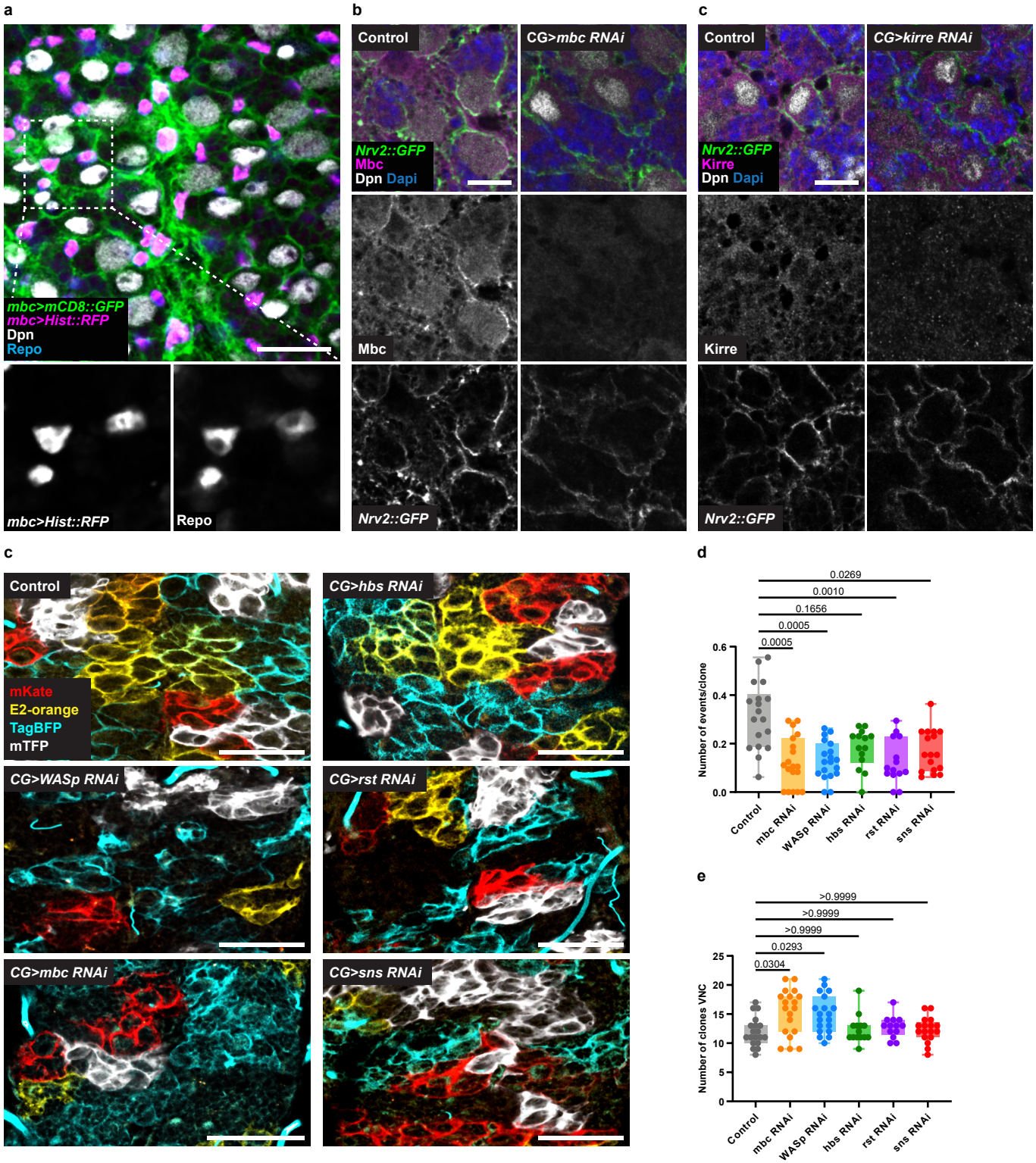

Rujano et al. Figure 6